OPEN ACCESS



A Stability Timescale for Nonhierarchical Three-body Systems

Eric Zhang ^{1,2,3}, , Smadar Naoz ^{1,2}, and Clifford M. Will ^{4,5}, Department of Physics and Astronomy, University of California, Los Angeles, CA 90095, USA; ezhang 951@gmail.com

² Mani L. Bhaumik Institute for Theoretical Physics, Department of Physics and Astronomy, UCLA, Los Angeles, CA 90095, USA

³ Department of Physics and Astronomy, University of California, Riverside, CA, 92507, USA

⁴ Department of Physics, University of Florida, Gainesville, FL 32611, USA

⁵ Institut d'Astrophysique, Sorbonne Université, 75014 Paris, France

**Received 2023 January 17; revised 2023 April 20; accepted 2023 May 15; published 2023 July 20

Abstract

The gravitational three-body problem is a fundamental problem in physics and has significant applications to astronomy. Three-body configurations are often considered stable as long the system is hierarchical; that is, the two orbital distances are well-separated. However, instability, which is often associated with significant energy exchange between orbits, takes time to develop. Assuming two massive objects in a circular orbit and a test particle in an eccentric orbit, we develop an analytical formula estimating the time it takes for the test particle's orbital energy to change by an order of itself. We show its consistency with results from *N*-body simulations. For eccentric orbits in particular, the instability is primarily driven not by close encounters of the test particle with one of the other bodies, but by the fundamental susceptibility of eccentric orbits to exchange energy at their periapsis. Motivated by recent suggestions that the galactic center may host an intermediate-mass black hole (IMBH) as a companion to the massive black hole Sgr A*, we use our timescale to explore the parameter space that could harbor an IMBH for the lifetime of the S-cluster of stars surrounding Sgr A*. Furthermore, we show that the orbit of an S-star can be stable for long timescales in the presence of other orbital crossing stars, thus suggesting that the S-cluster may be stable for the lifetimes of its member stars.

Unified Astronomy Thesaurus concepts: High energy astrophysics (739); Galaxies (573); Galactic center (565); Intermediate-mass black holes (816); Supermassive black holes (1663); Three-body problem (1695); Black holes (162); Exoplanets (498)

1. Introduction

The stability of triple-body systems is a pervasive problem in astrophysics. The three-body problem describes the dynamics of systems ranging from planetary systems to the orbits of stars and compact objects. A *stable* bound three-body system is loosely defined as one in which the energy of each orbit stays roughly the same, and *instability* is associated with systems in which the two orbits exchange energy. As a dramatic example, a bound orbit in a three-body system becomes unbound if its energy changes from negative to positive, and such systems are said to be unstable. Another example for instability can be considered an exchange process between the two orbits, which also dramatically changes the energy of each orbit.

The general approach in the literature often relies on a criterion by which the system could be considered stable *in the long run*. A common approach to developing such criteria is to designate hierarchical systems, or those in which the two orbital distances are well-separated, as long-term stable. The question of stability is then equivalent to determining a critical distance between the two orbits, where the system switches from hierarchical to nonhierarchical.

The most straightforward such criterion involves the Hills mechanism (Hills 1988). For a system composed of a binary and a tertiary, the Hills critical distance is the separation between the tertiary and the inner binary at which the tertiary's gravitational potential exceeds the primary's gravitational

Original content from this work may be used under the terms of the Creative Commons Attribution 4.0 licence. Any further distribution of this work must maintain attribution to the author(s) and the title of the work, journal citation and DOI.

potential. In this case, the secondary body in the inner binary may hop between the primary and the tertiary, yielding a new configuration of a tertiary–secondary and a primary. In the coplanar case, the functional expression of this place represents the first Lagrange point, which indicates the position where the gradient of the potential in the rotating frame is zero (e.g., Murray & Dermott 2000; Binney & Tremaine 2008). A stability criterion may be obtained by requiring that the tertiary is never closer to either of the other bodies than the Hills critical distance. The criterion has been improved by Hamilton & Burns (1991), Grishin et al. (2016).

The stability of three massive objects has a generalized, hierarchy-based stability condition often used in the literature (e.g., Mardling & Aarseth 2001), and similar stable–unstable boundaries were derived by Eggleton & Kiseleva (1995), Petrovich (2015), Tory et al. (2022), Vynatheya et al. (2022), and Hayashi et al. (2022). Considering hierarchical systems, where one mass orbits on a tight configuration about the primary and a tertiary is on a wider orbit, a condition is often used to estimate the long-term stability against high-eccentricity excitations due to secular dynamics (e.g., Ivanov et al. 2005; Lithwick & Naoz 2011; Katz & Dong 2012; Antonini et al. 2014; Bode & Wegg 2014; Naoz & Silk 2014) and nonsecular perturbations to secular dynamics (e.g., Antognini et al. 2014; Luo et al. 2016; Grishin et al. 2018; Bhaskar et al. 2020).

However, instability is a time-sensitive concept, and not every nonhierarchical system is instantaneously unstable. Mylläri et al. (2018) noted the dependence of stability on time, albeit without an explicit timescale. Additionally, Mushkin & Katz (2020) developed a stability timescale for

the outer orbit in hierarchical systems, based on formulae for secular energy exchange (e.g., Roy & Haddow 2003). Further studies on the time-dependence of stability were done by Hayashi et al. (2022, 2023), using *N*-body simulations of mildly hierarchical triples.

In this paper, we develop an analytical stability timescale, expanding the parameter space to nonhierarchical systems. We consider three-body systems consisting of a primary and companion of masses m_p and m_c , respectively, on a circular orbit, and a test particle m_t ($m_p > m_c \gg m_t$), on a highly eccentric orbit either about the primary body or about the massive binary as a whole, such that the system is not necessarily hierarchical. We denote these two cases the external companion and internal companion cases, respectively. Interestingly, the stability of such systems is primarily sensitive to a single parameter, α , defined as the ratio of the periapsis distance of the test particle to the companion's semimajor axis:

$$\alpha = \frac{r_{\text{peri}}}{a_c} = \frac{a_t(1 - e_t)}{a_c},\tag{1}$$

where a_t and e_t are the semimajor axis and eccentricity of the test particle's orbit. The system is most unstable for $\alpha = 1$, when the companion orbits at the same distance as the test particle's periapsis.

We derive our stability timescale based on how long it takes for the test particle's orbital energy to change. We also show that the changes in energy are driven by the fundamental susceptibility of the eccentric test particle to energy changes at its periapsis, and not by close encounters with the companion or the primary. Notably, we do not use the secular approximation, in which the phases of each orbit are averaged over timescales much longer than each orbital period, or any perturbations to the secular approximation. In that approximation, often used to describe the evolution of hierarchical systems, the long-term change in the energy of each orbit is zero. Thus, in order to explore the instability associated with orbital energy exchange, which is a feature of nonhierarchical systems, we must describe systems by other means.

In particular, we are motivated by the configuration at the center of our galaxy, which includes many crossing orbits. As an example, we focus on the hypothetical existence of an intermediate-mass black hole (IMBH) that may orbit around the supermassive black hole (SMBH). The existence of such an IMBH has been investigated based on a combination of theoretical and observational studies (e.g., Hansen & Milosavljević 2003; Maillard et al. 2004; Gürkan & Rasio 2005; Gualandris & Merritt 2009; Chen & Liu 2013; Fragione et al. 2020; Generozov & Madigan 2020; GRAVITY Collaboration et al. 2020; Naoz et al. 2020; Zheng et al. 2020; Rose et al. 2022). The IMBH may have a crossing orbit with the wellstudied star, S0-2. This star is located close to the SMBH Sgr A*. It has an orbital period of 16 yr and an eccentricity of about 0.88. The recent closest approach of this star has been used to test and confirm the prediction of general relativity for the relativistic redshift (e.g., GRAVITY Collaboration et al. 2018; Do et al. 2019) and the advance of the periapsis (GRAVITY Collaboration et al. 2020). Thus, in principle, S0-2 may be used to constrain the possibility of the existence of such an IMBH. In addition, much of the S-star cluster orbits Sgr A* at similar distances, with many potential orbital crossings (e.g., Ghez et al. 2005; Gillessen et al. 2009; Yelda et al. 2014). One may

wonder how unstable these orbits truly are, and if the S-star cluster is in fact a stable configuration.

The paper is organized as follows: We develop in Section 2 an analytic timescale $T_{\rm stab}$ for the time it takes for the energy of the test particle to change significantly. In Section 3, we then adopt, as a proof of concept, the possible existence of an intermediate-mass black hole (IMBH) at the center of our galaxy, which we treat numerically, and compare the results with the analytic timescale. In Section 4, we discuss applications of our timescale to various astrophysical settings. Finally, in Section 5, we summarize our results.

2. Analytic Stability Timescale

In this section, we present an analytic derivation of the stability timescale. For pedagogical purposes, we derive the timescale using two approaches: via the test particle's energy evolution, and via its semimajor axis evolution. The two quantities are defined by the equation

$$E = \frac{1}{2}v^2 - \frac{GM}{r} = -\frac{GM}{2a_t},\tag{2}$$

where E is the (specific) energy⁶ of the test particle's orbit, a_t is the test particle's semimajor axis, M is the mass of the central body or system, r is the distance between the test particle and the central body, and v is the velocity vector of the test particle relative to the central body. By this relation, the energy and semimajor axis contain the same information, so that the a change in one of the quantities by a given factor necessarily accompanies a change in the other by the same factor.

Throughout the derivation, and the remainder of the paper, we adopt the following notation: the masses of the primary, companion, and test particle will be denoted by m_p , m_c , and m_t respectively. The semimajor axis, eccentricity, inclination, longitude of ascending node, argument of periapsis, and true anomaly of both orbits will be denoted by a, e, ι , Ω , ω , and f, with a subscript c indicating the companion's orbital elements, and the subscript t indicating the test particle's orbital elements. The companion's and test particle's orbital periods are denoted P_c and P_t , respectively.

We fix the origin at the center of mass of all three bodies. Note that, as $m_t \to 0$, this is equivalent to the center of mass of the primary and companion. Position vectors of each of the bodies will be denoted by \mathbf{r} , and velocity vectors will be denoted by \mathbf{v} , with subscripts p, c, and t for the primary, companion, and test particle. The relative position and vectors between bodies are denoted by $\mathbf{r}_{ij} = \mathbf{r}_i - \mathbf{r}_j$, where i and j are the subscripts of the bodies. The relative velocity vectors are similarly denoted by \mathbf{v}_{ij} . We will write r and v for the magnitudes of these vectors.

As stated in the introduction, we assume a mass hierarchy between the three bodies, $m_p > m_c \gg m_t$, with $m_t \to 0$ as it is a test particle. We assume a highly eccentric⁷ test-particle orbit and a circular companion orbit ($e_c = 0$).

Because we are working in the nonhierarchical regime, where the orbital distances are not well-separated, defining the orbits of the companion and the test particle can be ambiguous.

⁶ This definition of the energy includes only the binding energy between the test particle and the central body, and ignores the interaction energy with other bodies. This definition of the orbital energy allows the second equality, involving the osculating semimajor axis a_t , to hold.

 $e_t \gtrsim 0.5$; see Appendix A for a discussion of the low-eccentricity regime.

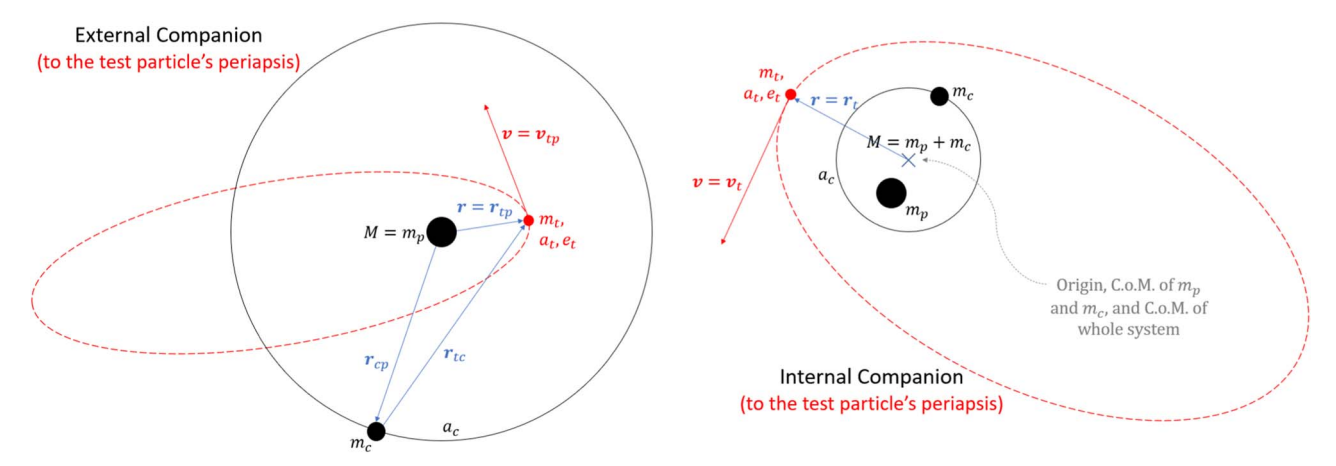


Figure 1. An illustration of the possible configurations. Left panel: a system where the companion orbits external to the test particle's periapsis. The central body is the primary, so that the test particle's orbital elements are defined via the position vector $\mathbf{r} = \mathbf{r}_{tp}$, and the velocity vector $\mathbf{v} = \mathbf{v}_{tp}$. Right panel: an internal companion. The effective central *body* is at the center of mass of the primary and the companion, and is fixed at the origin. The test particle's orbit is calculated using $\mathbf{r} = \mathbf{r}_{tp}$, and $\mathbf{v} = \mathbf{v}_{tp}$.

In particular, the mass of the central body, M, defined in Equation (2), depends on the configuration of the system. We define the companion's orbit to be external (internal) to the test particle's orbit if its semimajor axis, 8a_c , is greater (less) than the test particle's periapsis distance, $r_{\rm peri} = a_t(1 - e_t)$. If the companion is external, then the test particle's orbit is calculated with respect to the primary, and the central mass is $M = m_p$. If the companion is internal, then the test particle's orbit is calculated with respect to the center of mass of the primary and the companion, i.e., the origin, and the central mass is $M = m_p + m_c$. Figure 1 shows the two possible configurations.

2.1. Energy Approach

Our derivation is based on the realization that, when the test particle has a highly eccentric orbit, its energy is especially susceptible to gravitational perturbations near its periapsis. Accordingly, to evaluate the effect of these encounters, we approximate the energy evolution as a series of discrete, small jumps, where the jumps occur at each periapsis passage. The energy may either increase or decrease at each jump, depending upon the location of the companion body at that time, and so we treat its evolution as a random walk. We justify these assumptions analytically later in this section, and numerically in Section 3.

Indeed, it is possible for the test particle to undergo a large change in its energy while it is not at its periapsis, such as in the case of a close encounter between the test particle and the companion, e.g., if the test particle enters within a few Hill radii of the companion. However, for the purposes of our analytic derivation, we will ignore the effect of such events, which are arguably much rarer than periapsis passages. In principle, this assumption could cause our analytic timescale to overestimate the stability of the system, but our numerical results in Section 3 indicate that this is, in general, not the case.

Considering only small jumps in the energy, the energy evolves in a diffusive manner, as previously assumed. Although the expected overall energy change after N jumps averages to zero, the mean-square energy change is nonzero. This behavior leads to a spread in the distribution of possible energies after N periapsis passages, so that, for sufficiently

large N, it is probable that the energy has changed significantly, and thus, the system has become unstable. In particular, we say that the energy has changed significantly when the standard deviation σ of the distribution of energy changes ΔE after N periapsis passages is comparable to the initial energy itself—in other words, when

$$\sigma(\Delta E) = \sqrt{N}\sigma(\delta E) \sim E,\tag{3}$$

where $\sigma(\delta E)$ denotes the standard deviation of the distribution of energy jumps δE over a single periapsis passage.

The change in energy over any short time interval is given by

$$\delta E = \frac{\partial E}{\partial \mathbf{v}} \cdot \delta \mathbf{v} = \mathbf{v} \cdot \mathbf{f}_{\text{pert}} \, \delta t, \tag{4}$$

where $f_{
m pert}$ is the perturbing force (per unit test mass) due to the companion's presence. From this equation, we see that the energy change over any short time interval depends only on two quantities: the test particle's speed (or magnitude of its velocity), and the component of the perturbing force directed along the velocity vector, $f_{\text{pert}}^{\parallel}$. For highly eccentric orbits, the speed will be much greater near periapsis than at other times in the orbit. On the other hand, the force component $f_{\text{pert}}^{\parallel}$ depends strongly on the relative position of the test particle and companion, which varies quasi-randomly so that $f_{\text{nert}}^{\parallel}$ does not peak reliably. In particular, the parallel component of the force takes on essentially random values each time the test particle approaches its periapsis. Thus, our initial assumptions are justified; jumps primarily drive the change in energy at periapsis, and such jumps will behave like a random walk. The standard deviation of the distribution of energy changes is estimated by the scale of these changes, i.e.,

$$\sigma(\delta E) \sim v_{\text{peri}} | f_{\text{pert}} | \delta t.$$
 (5)

We note that this depends only on the vector magnitudes, since the relative orientation of the vectors controls the sign and the relative strength of each energy jump, but not their overall scale.

Then Equation (3) can be solved for N to obtain the number of test-particle orbits before a significant energy change occurs. Noting that the stability timescale T_{stab} is of order NP_t , we may

 $^{^8\,}$ Since the companion's orbit is circular, a_c is the same as the orbital distance, which is constant.

find T_{stab} via the expression

$$\frac{T_{\text{stab}}}{P_t} \sim \frac{E^2}{v_{\text{peri}}^2 |f_{\text{pert}}|^2 \delta t^2},\tag{6}$$

from which we may obtain T_{stab} in terms of known orbital parameters by estimating each of the terms E, v_{peri} , $|f_{\text{pert}}|$, and δt for various regimes.

The energy, E, is given by Equation (2), and v_{peri} can be estimated by the periapsis velocity of the test particle in a standard Keplerian orbit, given by

$$v_{\text{peri}} \approx \sqrt{\frac{GM}{a_t} \frac{1 + e_t}{1 - e_t}},\tag{7}$$

where, as in Equation (2), $M = m_p$ for external companions, and $M = m_p + m_c$ for internal companions.

Depending on whether the companion is external or internal, there are two possible expressions for the perturbing force, f_{pert} . When the companion is external, the perturbing force is given by

$$f_{\text{pert}} = -\frac{Gm_c r_{\text{tc}}}{r_{\text{tc}}^3} - \frac{Gm_c r_{\text{cp}}}{r_{\text{cp}}^3},$$
 (8)

where the first term is the gravitational force on the test particle from the companion, and the second term is due to the noninertial motion of the primary about the primary-companion mutual center of mass. Under the approximation that the majority of the encounters are weak, and noting that $a_c > r_{\rm peri}$ for external companions, the distance between the two bodies, r_{tc} , will typically be on the order of a_c . In particular, $r_{tc} \sim r_{cp} \sim a_c$, so that the magnitude of the total perturbing force can be estimated as

$$|f_{\text{pert}}| \sim \frac{Gm_c}{a_c^2}.$$
 (9)

When the companion is internal, we calculate the test particle's orbit with respect to the center of mass of the primary and companion. In this case, $f_{\rm pert}$ is

$$f_{\text{pert}} = -\frac{Gm_p r_{\text{tp}}}{r_{\text{tp}}^3} - \frac{Gm_c r_{\text{tc}}}{r_{\text{tc}}^3} + \frac{G(m_p + m_c)r_t}{r_t^3},$$
 (10)

where the first two terms are the total gravitational force on the test particle, and the third term subtracts the nonperturbing component from the total force from the primary and companion, respectively. The magnitude of the perturbing force is best estimated by the leading-order multipole term of the force, which is the quadrupole force. Thus, we can approximate the magnitude of Equation (10) as⁹

$$|f_{
m pert}| \sim \frac{Gm_p m_c a_c^2}{Mr_{
m peri}^4}.$$
 (11)

Roughly speaking, one can consider two possible cases for the interaction interval δt . The first is the aforementioned periapsis interval, under the approximation that the most significant perturbations (though still weak) occur over some interval of time at which the test particle is near its periapsis, $T_{\rm peri}$. Since the test particle's susceptibility to energy exchange

is determined by its velocity (as per Equation (4)), we estimate the length of this interval by the time integral of the cross-track component of the relative test-particle velocity, v_{ϕ} , over one period of its orbit, divided by its maximum value, i.e.,

$$T_{\text{peri}} = \int_0^{P_t} \frac{v_{\phi}}{v_{\phi,\text{max}}} dt = (1 - e_t) P_t.$$
 (12)

If the companion does not move significantly during the interval of periapsis passage, then the perturbing force can be treated as constant over $T_{\rm peri}$. In this case, the energy change over the whole periapsis passage is well described by an impulse approximation, and the interaction interval δt is the same as $T_{\rm peri}$.

On the other hand, if the companion moves during the test particle's periapsis passage, we can no longer use the impulse approximation. In particular, if the companion's period is sufficiently short, it may complete a significant fraction of its orbit while the test particle is at periapsis, so that the perturbing force $f_{\rm pert}$ cannot be regarded as constant over the interval $T_{\rm peri}$. In this case, the impulse approximation is, strictly speaking, invalid. Nonetheless, an interaction timescale δt can still be estimated. In this case, we evaluate the change in energy per periapsis passage by dividing the interval of periapsis passage into shorter intervals, dt, for which the perturbing force is constant. Then, by integrating over each of these intervals, the total energy change, δE , is

$$\delta E = \mathbf{v} \cdot \int_{t_i}^{t_f} f_{\text{pert}} dt = v_{\text{peri}} \int_{t_i}^{t_f} f_{\text{pert}}^{\parallel} dt, \qquad (13)$$

where $[t_i, t_f]$ is the interval of periapsis passage, and f_{pert}^{\parallel} is the component of the perturbing force parallel to the test particle's velocity during the interaction. Thanks to the companion's circular orbit, this component of the force varies roughly sinusoidally with the companion's mean anomaly, so that it may be approximated as

$$f_{\text{pert}}^{\parallel} \sim |f_{\text{pert}}| \cos n_c t,$$
 (14)

where n_c is the mean motion of the companion. Then Equation (13) can be approximated as

$$\delta E \sim v_{\text{peri}} \int_{t_i}^{t_f} |\mathbf{f}_{\text{pert}}| \cos n_c t dt$$

$$= v_{\text{peri}} n_c^{-1} |\mathbf{f}_{\text{pert}}| \sin n_c t|_{t_i}^{t_f} \sim v_{\text{peri}} n_c^{-1} |\mathbf{f}_{\text{pert}}|, \qquad (15)$$

where the sine term represents the dependence on the orientation and thus causes the spread in the distribution of possible δE . From Equation (15), it follows that the interaction timescale when the companion's period is short is

$$\delta t \sim n_c^{-1} = \frac{P_c}{2\pi}.\tag{16}$$

In general, the interaction timescale is given by the shorter of the two cases,

$$\delta t \sim \min\left(T_{\text{peri}}, \frac{P_c}{2\pi}\right),$$
 (17)

so that the former (latter) value is used if the companion's movement is (is not) negligible over the periapsis interval.

There are three regimes to consider when evaluating Equation (6): (1) external companion with a long period, (2) external companion with a short period, and (3) internal

A more detailed derivation of this estimate can be found in Appendix B.2.

Table 1 A Summary of Estimates of M, $|f_{\text{pert}}|$, and δt for Each Regime

Regime	Companion Orbit	Companion Period	М	f _{pert}	δt
$r_{\text{peri}} < a_c, T_{\text{peri}} \ll P_c$	External	Long	m_p	Gm_c/a_c^2	$T_{ m peri}$
$r_{ m peri} < a_c, \ T_{ m peri} \gtrsim P_c$	External	Short	m_p	Gm_c/a_c^2	$P_c/2\pi$
$r_{ m peri} > a_c, \ T_{ m peri} \gtrsim P_c$	Internal	Short	$m_p + m_c$	$Gm_p m_c a_c^2 / Mr_{\rm peri}^4$	$P_c/2\pi$

Note. $|f_{pert}|$ is given by Equations (9) and (11), and δt is given by Equation (17).

companion with a short period. The three possible cases are summarized in Table 1. Note that Kepler's law $P_c \propto a_c^{3/2}$ forbids the case of an internal companion with a long period.

Evaluating Equation (6) for the two external companion cases and the one internal companion case then gives

$$\frac{T_{\text{stab}}}{P_t} \sim \frac{q^{-2}}{4(1+e_t)} \times \begin{cases}
\alpha^{-4}(1-e_t)^3/(2\pi)^2 & T_{\text{peri}} < P_c/2\pi, \ \alpha < 1 \\
\alpha^{-1}(1-e_t)^2(1+q) & T_{\text{peri}} > P_c/2\pi, \ \alpha < 1, \\
\alpha^7(1-e_t)^2(1+q)^4 & \alpha \geqslant 1
\end{cases}$$
(18)

where q is the mass ratio m_c/m_p , and $\alpha = a_t(1 - e_t)/a_c$ (see Equation (1)).

2.2. Semimajor Axis Approach

The energy of the test-particle orbit is proportional to the inverse of its osculating semimajor axis; that is, $E \propto a_t^{-1}$. Thus, a change in E by an order of itself necessarily means that a_t has changed by an order of itself as well. Similar to Equation (4), a significant change in the test particle's semimajor axis occurs when

$$\sigma(\Delta a_t) = \sqrt{N}\,\sigma(\delta a_t) \sim a_t. \tag{19}$$

The change in semimajor axis at each periapsis passage, δa_t , can be estimated by

$$\delta a_t \approx \frac{da_t}{dt}|_{\text{peri}} \delta t,$$
 (20)

where da_t/dt , given by the Lagrange planetary equation for semimajor axis evolution (e.g., Murray & Dermott 2000; Poisson & Will 2014; where we adopt similar notation to Will 2021), is as follows:

$$\frac{da_t}{dt} = 2\sqrt{\frac{a_t^3}{GM(1 - e_t^2)}} \times \{e_t \sin f_t \mathbf{f}_{pert} \cdot \hat{\mathbf{i}} + (1 + e_t \cos f_t) \mathbf{f}_{pert} \cdot \hat{\mathbf{j}} \}, \quad (21)$$

where \hat{i} and \hat{j} are the radial and cross-track unit vectors of the test particle with respect to the central body.

Given the interaction timescale mentioned above (Equations (12) and (16)), δa_t is, at periapsis,

$$\delta a_t \approx 2\sqrt{\frac{a_t^3(1+e_t)}{GM(1-e_t)}}f_{\text{pert}}\cdot\hat{\boldsymbol{j}} \delta t.$$
 (22)

Information about the relative orientation of the two orbits is contained by the $f_{\text{pert}} \cdot \hat{j}$ term. The standard deviation of the

Table 2
The Relevant Numerical Initial Conditions

Label	$m_c~(M_\odot)$	a_c (au)	r _{peri} (au)	e_t	No. Runs
DiffComp	$50-10^6$	10-10 ⁴	118.32	0.884	8308
DiffTestP	5000	100	16-4000	0.2 – 0.997	18,440

Note. The results are shown in Figures 3 and 5. Note that in these figures the square points represent an average over 10 realizations in terms of the initial orbital angles, $\omega_{c,t}$, $\Omega_{c,t}$, $i_{c,t}$, and $f_{c,t}$.

distributions of possible δa_t is then on the order of

$$\sigma(\delta a_t) \sim 2\sqrt{\frac{a_t^3(1+e_t)}{GM(1-e_t)}} |f_{\text{pert}}| \delta t, \qquad (23)$$

which, when plugged into Equation (19), for the various cases of $|f_{pert}|$ and δt , yields the same timescale as Equation (18).

3. Comparison with Numerical Results

3.1. Description of the Initial Conditions and the Numerical Approach

As a proof of concept, we consider a system consisting of the galactic center black hole Sgr A* as the primary mass m_p , a star in orbit around Sgr A* as the test particle m_t , and a hypothetical IMBH companion to Sgr A* as the companion m_c . Using HNBody (Rauch & Hamilton 2002), we directly integrate over 26,000 variations of this system assuming Newtonian gravity. From the results, we may calculate $T_{\rm stab}$ numerically by finding the first time at which the test particle's semimajor axis (energy) changes by a factor of 2 from its initial value. Comparing this value to the analytic prediction then provides a test of the analytic timescale. We note that not every destabilization, as defined above, necessarily leads to an ejection of the particle from the system. An ejection occurs when the energy changes from negative to positive (i.e., $\Delta E > + E$), and is thus a subset of destabilization.

We run a grid of systems, varying the IMBH mass and separation. In all runs, we use $m_p = 4 \times 10^6 \, M_{\odot}$, and $m_t = 10 \, M_{\odot}$, and set the companion's eccentricity to $e_c = 10^{-3} \approx 0.11$ We present two sets of numerical runs, as summarized in Table 2. In the runs labeled DiffComp, we set the test particle's initial orbital parameters to be the same in all

We do not include any post-Newtonian (pN) precession for the purposes of this comparison. The first pN precession can stabilize the system against secular perturbations (e.g., Naoz et al. 2013b) even in the cases where the orbits are more compact than that of the hierarchical limit (e.g., Faridani et al. 2022; Wei et al. 2021). However, the purpose of this numerical analysis is to test our analytical timescale.

¹¹ When $e_c = 0$ exactly, the argument of periapsis ω_c is ill-defined. Eccentricities of exactly zero are unlikely in practice, so we avoid this pathological case by setting $e_c = 10^{-3}$.

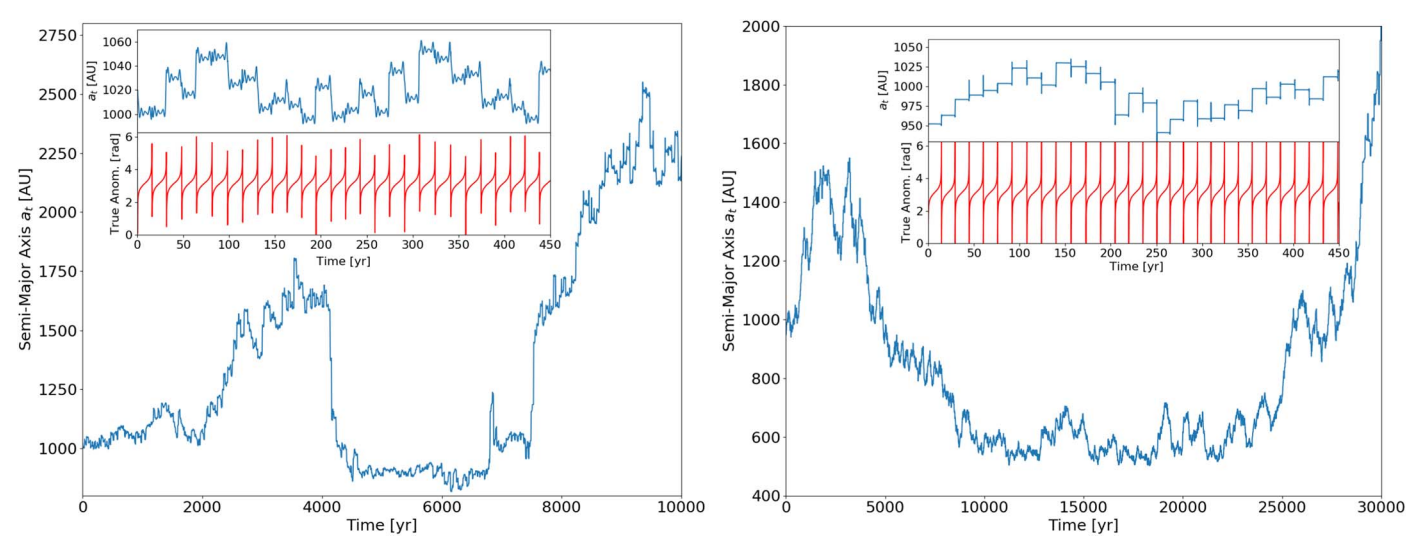


Figure 2. Sample time evolution of the test particle's semimajor axis. The semimajor axis evolution contains the same information as the energy evolution. Left panel: external companion. An external companion IMBH of 9000 M_{\odot} orbiting Sgr A* at 380 au, and a test-particle star orbiting Sgr A* with an initial semimajor axis of 1020 au and eccentricity of 0.884. The semimajor axis can increase and decrease with no clear bias, thus justifying the approximation of the energy evolution as a random process. We also show a *zoomed in* time evolution of the same system. Substantive changes to the semimajor axis of the star only occur during the *peaks* in the true anomaly evolution, corresponding to the periapsis passage of the star. Right panel: internal companion. An internal companion IMBH of 27,000 M_{\odot} orbiting Sgr A* at 64 au, and a test-particle star orbiting the Sgr A*-IMBH binary with an initial semimajor axis of 1020 au and eccentricity of 0.884. The system's behavior is similar to the external case.

runs, namely those of the star S0-2, i.e., $a_t = 1020$ au, $e_t = 0.884$, and $m_t = 10~M_{\odot}$, and vary the companion's mass and semimajor axis systematically. The test particle's argument of periapsis, ω_t , longitude of ascending node, Ω_t , and inclination, ι_t , are chosen such that they will have the observed values of S0-2 on the sky, and then projected into the invariable plane. The companion for this set of runs is varied on a grid of $m_c \in [50, 10^6]~M_{\odot}$, and $a_c \in [10, 10^4]~au$.

In the second set of runs (labeled DiffTestP), we set the companion's mass and semimajor axis to be $m_c = 5000 \ M_{\odot}$, and $a_c = 100 \ \text{au}$, respectively, and its eccentricity to be $e_c = 10^{-3}$. In this case, we arbitrarily choose the inclination of the companion's orbit to be close to zero¹² (0.001 rad). This choice eliminates dependencies on the companion's argument of periapsis and longitude of ascending nodes. In this set of runs, the test particle's initial periapsis distance is then systematically varied from $a_t(1-e_t) \in [16, 4000]$, and its eccentricity from $e_t \in [0.2, 0.997]$.

When the orbital configurations are varied, in runs DiffComp or DiffTestP, we chose the initial longitudes of ascending nodes, arguments of periapsis, and mean anomalies from a uniform distribution between 0 and 2π , and the mutual inclination from an isotropic distribution (i.e., uniform in cosine).

In Section 3.2, we discuss the numerical time evolution of the test-particle orbit, and how it justifies the assumptions used in deriving the analytic timescale. In Sections 3.3 and 3.4, we separately analyze each set of numerical runs and compare them to the analytic timescale predictions.

3.2. Time Evolution of the Test-particle Orbit

The numerical results justify our approximation of the test particle's energy evolution as a series of discrete, random *jumps* occurring each time the test particle reaches its periapsis. Figure 2 depicts two representative cases of the test particle's

time evolution in the presence of an external and internal companion (left and right panels, respectively). In particular, the inset panels show a zoom-in on the part of the evolution that exhibits the energy jumps described in Section 2. These jumps occur at the test particle's periapsis, as indicated by the peaks in its true anomaly evolution. Moreover, Figure 2 demonstrates that over time the test particle's semimajor axis (energy) can increase and decrease in a diffusive manner so that its evolution is well described by a random process. We provide additional examples of the time evolution of the test particle's orbit in Appendix B (see Figure 8).

3.3. Dependence of the Timescale on the Companion Parameters

In the DiffComp set of runs, we integrated a total of 8308 configurations, initially starting with the same test-particle orbital configuration and varying systematically the orbit of the companion. All integrations are stopped at 10^7 yr.

As stated above, we record the time at which the test particle's energy has changed from its initial value by a factor of 2. The results are shown in the left-hand side of Figure 3, where the color coding shows the time at which the test particle's energy changed by a factor of 2, ranging from 1 to 10^7 yr. The systems whose test-particle energy never changes by a factor of 2 within 10^7 yr are depicted as a gray square. We depict this value as a function of the companion's semimajor axis a_c and mass m_c (filled circles in Figure 3). For each point on the grid, we initially run one system with a value of m_c and a_c . The top panel shows systems with an external companion $(a_c > r_{\rm peri})$, and the bottom panel shows systems with an internal companion $(a_c < r_{\rm peri})$.

On the right-hand side of Figure 3, we plot the fractional change in angular momentum (i.e., $\Delta L/L$) at $t=T_{\rm stab}$. The symbols have the same meaning as those from the left-hand side panel.

Note that, in the part of the parameter space where the system is very nonhierarchical $(a_c \sim r_{\rm peri})$ and where $m_c \ll m_p$,

When $\iota_c = 0$ exactly, the longitude of ascending node Ω_c is ill-defined.

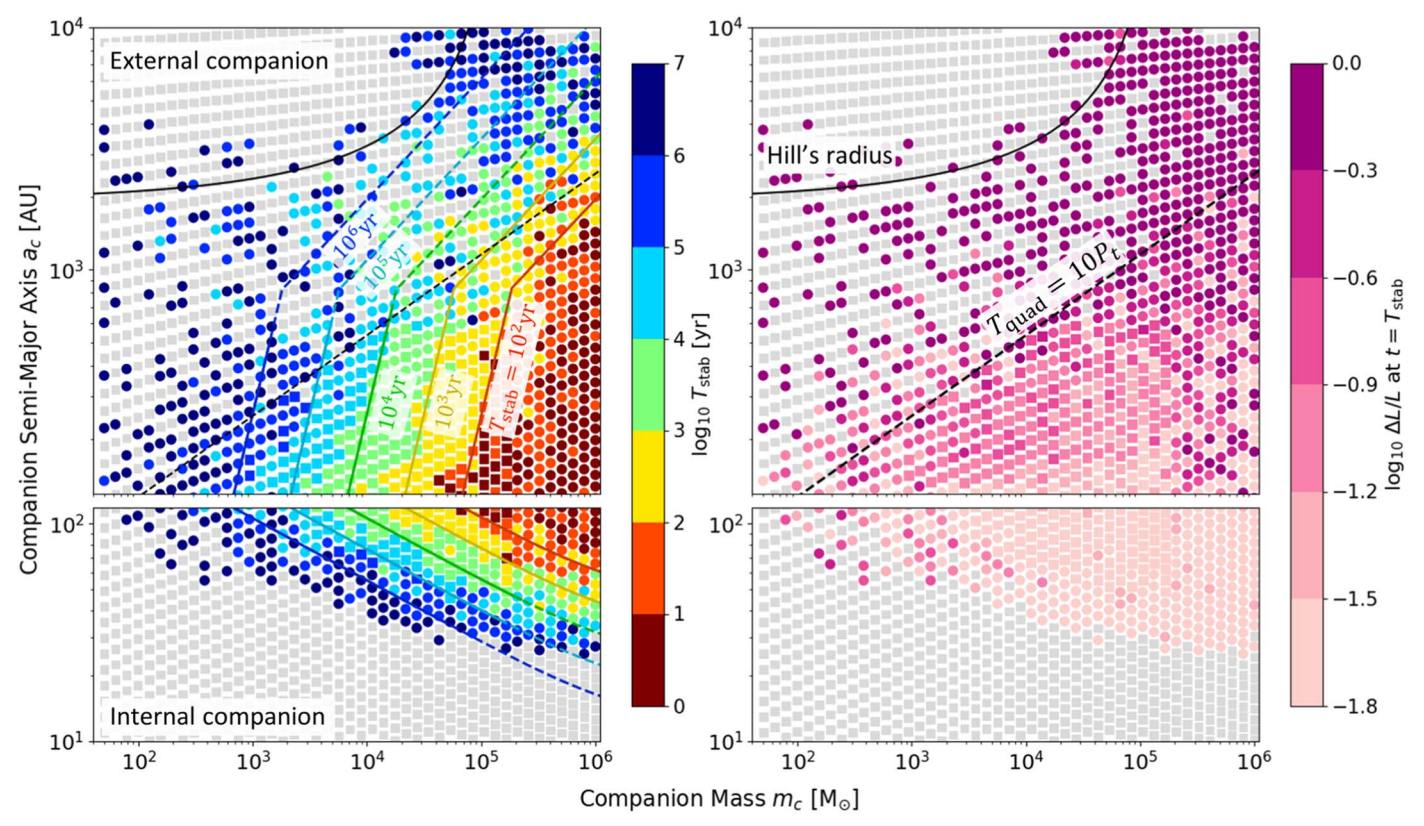


Figure 3. Stability timescale as a function of companion parameters. Left: $T_{\rm stab}$ as a function of the companion's semimajor axis a_c and its mass m_c , as determined by direct N-body integration. The upper (lower) panels describe an external (internal) companion. A colored dot represents a change in S0-2's energy by a factor of more than 2 within the maximum integration time of 10^7 yr, where the color determines $T_{\rm stab}$. A colored square represents 10 systems with the same m_c and a_c , such that all 10 systems have a change in the test-particle energy of more than a factor of 2 within the integration time. The color of the square is the geometric mean of $T_{\rm stab}$ over all 10 systems. A gray square represents no such change in the test-particle energy within the integration time. Overlaid are lines of constant $T_{\rm stab}$, as predicted by Equation (18). Some systems outside the regime where $T_{\rm stab} < 10^7$ yr still exhibit significant change in their orbit, if they are within the region where the test particle can enter the Hill sphere of the companion, i.e., below the solid black line. The dashed black line marks where the Kozai quadrupole timescale is 10 times greater than the test-particle period. Secular approximations are reasonably applicable for systems above this line, causing them to exhibit angular momentum oscillations, which can suppress the random walk nature of the energy evolution, leading to more stable systems than those predicted by the analytic timescale. Right: the normalized change in test-particle angular momentum at $t = T_{\rm stab}$. As predicted by the quadrupole timescale, systems above this line exhibit significant changes in angular momentum.

the dynamical behavior is rather chaotic (e.g., Stone & Leigh 2019; Ginat & Perets 2021a, 2021b; Kol 2021; Manwadkar et al. 2021). Therefore, in this part of the parameter space, we ran additional 10 configurations with the same values of m_c and a_c , and numerically calculated $T_{\rm stab}$ for these values by taking the geometric mean of the times at which the energy changes by a factor of 2. These grid points are marked as boxes in Figure 3. Overplotted are the contours of the analytic timescales from Equation (18).

For the majority of the parameter space, in particular where the system is *least hierarchical* ($\alpha \sim 1$), we find good agreement between the analytic and numeric results. This suggests both that our analytic result is a good estimate of the stability timescale and also that the instability is sufficiently explained by energy jumps at periapsis. Close encounters of the test particle with the other two bodies, while possible in principle, are evidently not frequent enough to drive the instability of the system in this regime.

There are two regions of the parameter space for which there is disagreement between the analytic and numerical results: systems above the black dashed line in Figure 3, which are more stable than predicted, and some systems to the left of the blue $T_{\rm stab}=10^6\,{\rm yr}$ line, which are less stable than expected.

In the former region, the semimajor axes of the two orbits are not well-separated, but the secular approximation is none-theless somewhat applicable. Thus, the semimajor axis evolution of these systems cannot be treated as random walks, as in Figure 2, but oscillations that are roughly consistent with secular behavior (i.e., quasi-secular).

As an example, we show the evolution of such a system in Figure 4. In this system, the energy (i.e., the semimajor axis) evolves not as a random walk, but as an oscillation, never straying far from its initial value. As expected, thanks to the eccentric Kozai–Lidov mechanism (Kozai 1962; Lidov 1962; Naoz et al. 2013a), the system also exhibits large oscillations in the test particle's angular momentum, shown in the upper region of the top right panel of Figure 3. These angular momentum oscillations take place roughly on the timescale of

$$T_{\text{quad}} \sim \frac{16}{30\pi} \frac{m_p + m_c + m_t}{m_c} \frac{P_c^2}{P_t} (1 - e_c^2)^{3/2}$$
 (24)

¹³ These energy oscillations are similar to those noted by Antognini et al. (2014), Luo et al. (2016), Grishin et al. (2016), Grishin et al. (2018), and Bhaskar et al. (2020), which take place roughly on an orbital timescale and may eventually cause nonsecular evolution.

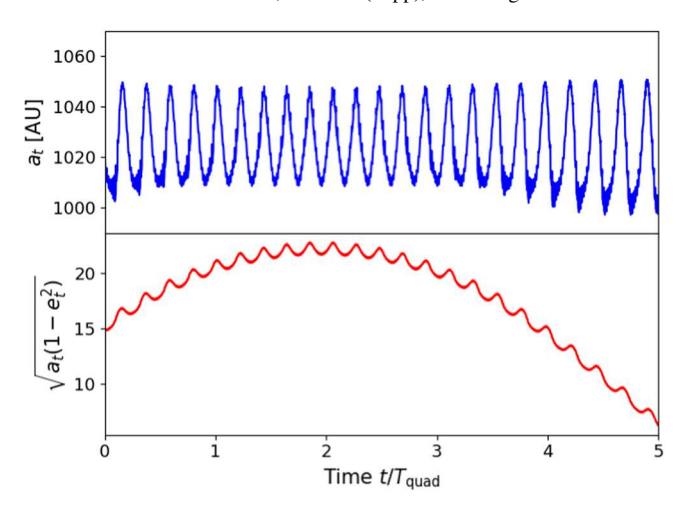


Figure 4. Time evolution of a sufficiently hierarchical system. A system consisting of an external IMBH with mass $9000~M_{\odot}$ orbiting Sgr A* at $a_c=980$ au, and a test-particle star with $a_t=1020$ au, $e_t=0.884$. Although the system is not strictly hierarchical, the system exhibits behavior predicted by the secular approximation. The test particle's semimajor axis does not evolve like a random walk, but instead oscillates. Large eccentric Kozai–Lidov oscillations in the test particle's angular momentum occur as well. Because the system does not behave like a random walk, the analytic timescale fails.

(e.g., Antognini 2015). The systems for which this timescale is much longer than the test particle's period, i.e., by a factor of $10~(T_{\rm quad}>10P_t)$, are typically governed by quasi-secular rather than random walk behavior. Thus, their stability is better described by secular criteria (e.g., Ivanov et al. 2005; Lithwick & Naoz 2011; Katz & Dong 2012; Antognini et al. 2014; Antonini et al. 2014; Bode & Wegg 2014; Naoz & Silk 2014; Luo et al. 2016; Grishin et al. 2018; Bhaskar et al. 2020). On the upper right panel of Figure 3, these systems are shown to have changes in angular momentum $\gtrsim 50\%$ and lie above the black dashed line.

For sufficiently large α (bottom panel, internal companion), the system is also hierarchical, so that secular approximations can likewise be applied, and the energy does not behave like a random walk. Here, we expect that the secular inverse eccentric Kozai–Lidov mechanism (Naoz et al. 2017, 2020) or the hierarchical stability timescale of Mushkin & Katz (2020) provides a better stability criterion.

In the latter region, some systems undergo changes in their orbital energy on shorter timescales than those predicted by our analytical criterion. In such cases, close encounters between the test particle and another body are important to the system's evolution. Such close encounters may only occur if the star's apoapsis is within a few Hill radii of the IMBH's orbit. This condition can be expressed as

$$a_c < a_t(1+e_t) + kR_{\text{Hill}},\tag{25}$$

where $R_{\rm Hill}$ is the Hill radius of the companion, defined as

$$R_{\text{Hill}} = a_c \left(\frac{m_c}{m_p}\right)^{1/3},\tag{26}$$

and k is a factor of order unity (similarly to planet–planet scattering, e.g., Chatterjee et al. 2008). In Figure 3, this condition is shown as the solid black curve (where we adopt k=3). Indeed, systems above this curve very rarely exhibit a large change in energy. While such systems in which close

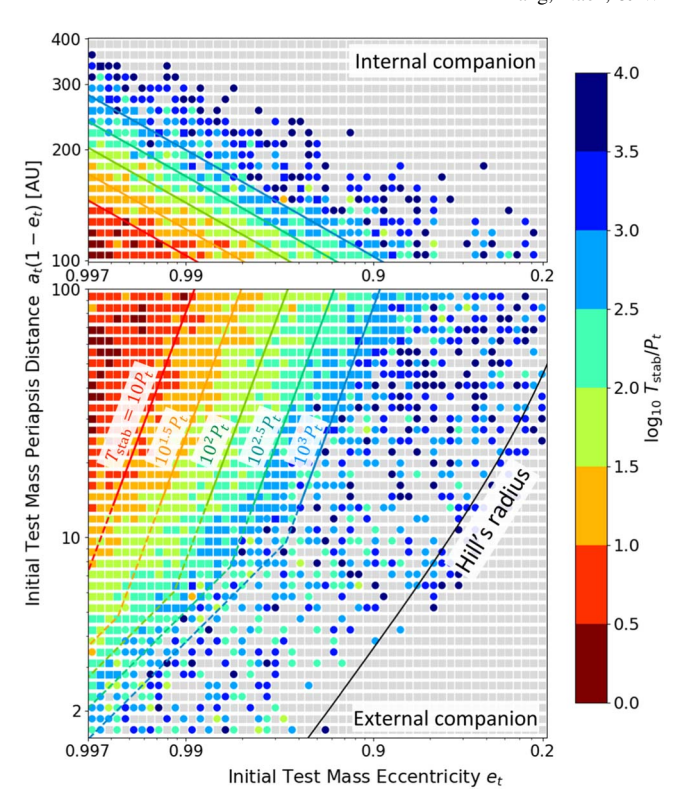


Figure 5. Stability timescale as a function of test-particle parameters. Note that, unlike in Figure 3, we vary the test particle's orbital parameters, not the companion's parameters, and thus, the positions of the external and internal cases are flipped. The meaning of the symbols is the same as in Figure 3. The solid black line shows the Hill sphere boundary; very few systems below this line exhibit a significant energy change within the maximum integration time of 10^4 test-particle periods.

encounters are important do exist, they are relatively few and far between in Figure 3, whereas the general trend in Figure 3 obeys the timescale as predicted by energy jumps at periapsis. This provides further evidence that energy jumps at periapsis, not close encounters, are the primary drivers of instability.

3.4. Dependence of the Timescale on the Test-particle Parameters

In this set of runs, DiffTestP, we integrated a total of 18,440 configurations, this time starting with the same companion parameters (see Table 2) and systematically varying the parameters of the test particle. We again record the first time at which the test particle's energy changes by a factor of 2, and depict this time as a function of the initial test-particle periapsis distance $r_{\rm peri}$ and its eccentricity e_t . We integrated each system for 10^4P_t , where P_t is the initial test-particle period. Similarly, as for the DiffComp run, we run an additional 10 realizations for systems that have $\alpha \sim 1$. The results are shown in Figure 5. The color code here represents the time for changing the energy by an order of itself, normalized by the test-particle period, i.e., $T_{\rm stab}/P_t$. In Figure 5, the internal case is shown in the top panel, and the external case is shown in the bottom panel.

We again find good agreement between the analytic and numerical results. As in DiffComp, we find that the analytic and numerical timescales agree for a majority of the parameter space. Similarly to the DiffComp set of runs, the agreement with the analytic timescale is best in the regime $\alpha \sim 1$, while the analytic timescale begins to fail in the regimes $\alpha \gg 1$ or

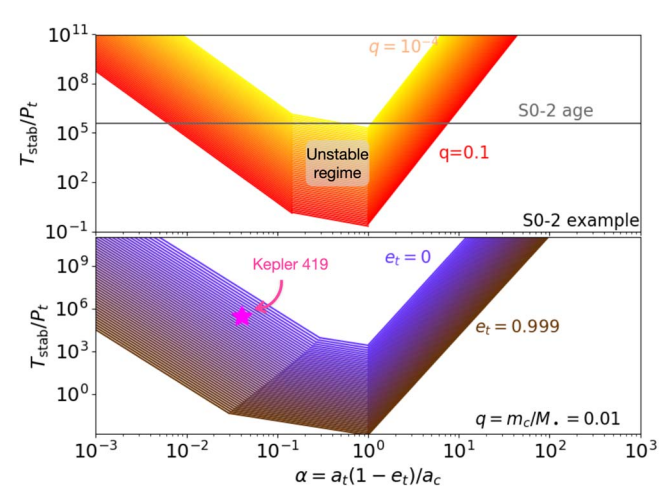


Figure 6. Stability parameter. Top: number of stable orbits of S0-2 as a function of α , for companion-primary mass ratios between 10^{-4} and 10^{-1} , assuming an eccentricity of 0.884 for S0-2. The gray line shows the age of S0-2. Regions where the gray line lies above a chosen colored line (corresponding to a given companion-primary mass ratio) are excluded values for α , as, in these cases, S0-2's orbit would be too unstable to survive to its current age. Bottom: number of stable orbits of a test particle with the same semimajor axis as S0-2 as a function of α for test-particle eccentricities ranging from 0 to 0.999, assuming a companion-primary mass ratio of 0.01 ($m_c = 4 \times 10^4 M_{\odot}$). The star in the bottom panel represents the approximate position of Kepler-419 (see text for discussion).

 $\alpha \ll 1$, i.e., when the system is hierarchical. Additionally, we see systems to the right of the blue $T_{\rm stab} = 10^3 \, P_t$ line, which become unstable much faster than the analytic timescale predicts, which we attribute to close encounters between the companion and the test particle.

4. Applications

4.1. The S-cluster in the Presence of an IMBH

Recent gravitational-wave observations by the LIGO-Virgo collaboration have now confirmed the existence of IMBHs (e.g., GW190521; The LIGO Scientific Collaboration et al. 2020a, 2020b). Specifically, our galactic center may harbor IMBHs as the result of a possible minor merger with a lowmass or dwarf galaxy, or even with a globular cluster. Such a scenario was considered by Rashkov & Madau (2014), who suggested that, if IMBHs serve as the seeds of SMBHs in the center of galaxies, hierarchical galaxy evolution would yield many IMBHs in our galaxy. Additionally, a combination of theoretical and observational arguments suggests that an IMBH is expected to exist in the central parsec of our galaxy (e.g., Hansen & Milosavljević 2003; Maillard et al. 2004; Gürkan & Rasio 2005; Gualandris & Merritt 2009; Chen & Liu 2013; Fragione et al. 2020; Generozov & Madigan 2020; Naoz et al. 2020; Zheng et al. 2020). Of particular interest are the proposed efficient formation of IMBHs as a result of black hole mergers (e.g., Fragione et al. 2022), or via black holes collisions with main-sequence stars (e.g., Rose et al. 2022).

To constrain the parameter space of mass and semimajor axis of a hypothetical IMBH, Naoz et al. (2020) used the long baseline of observations of the star S0-2, located close to the SMBH Sgr A*. S0-2 has been observed for more than two decades, and its orbit is sufficiently regular that, if there is a companion to Sgr A*, it is either quite close to the main black hole or well outside the orbit of S0-2.

The stability analysis done here (see Figure 3) suggests that the parameter space for which the orbit of S0-2 will be stable over its lifetime (6 Myr, Lu et al. 2013) is constrained to the left side of Figure 3. Another way to visualize the parameter space is depicted in Figure 6. In the top panel of Figure 6, we consider S0-2 parameters for a wide range of a companion semimajor axis and mass ratio (with respect to the SMBH's mass), depicted as the color-coded lines. The y-axis represents the stability timescale normalized to the period of S0-2. As shown in the figure, the stable regime for a given mass ratio q is wherever the corresponding colored line lies above the gray line denoting the age of S0-2. Thus, for example, for q = 0.1 $(m_c = 4 \times 10^5 \, M_{\odot})$, the allowed regions are $\alpha \lesssim 10^{-2}$ (companion IMBH well outside the periapsis of S0-2), and $\alpha \gtrsim 10$ (companion well inside the periapsis of S0-2). For $q = 10^{-4}$ $(m_c = 400 \, M_{\odot})$ (very low-mass companion), the orbit of S0-2 is stable for essentially any value of α .

4.2. The Stability of the S-star Cluster

The S-star cluster is a collection of stars on nearly isotropic orbits, within the innermost arcsecond of Sgr A* (e.g., Lu et al. 2009; Gillessen et al. 2012; Sabha et al. 2012). These stars are eccentric and orbit-crossing, and are estimated to be relatively young (e.g., Ghez et al. 2004, 2005; Gillessen et al. 2009; Lu et al. 2009; Gillessen et al. 2012; Lu et al. 2013; Yelda et al. 2014; Gillessen et al. 2017; Do et al. 2019). Thus, in the context of this investigation, the question of the stability of the S-cluster translates to the timescale of the stability. We simplify the question by considering perturbations to S0-2's orbit by other stars, one at a time.

Examining the top panel of Figure 6, we see that the low mass ratio curve $(q=10^{-4})$ implies that even an object as massive as $400\,M_\odot$ will be able to lurk in the presence of S0-2 without destabilizing its orbit during its lifetime. Thus, other stars, naturally, will not destabilize S0-2's orbit as well. We thus suggest that, during the lifetime of the S-cluster, star–star interactions do not change the stellar orbits' energies by order of themselves. ¹⁴

4.3. Stellar and Planetary Systems

Since the stability timescale developed here depends only on products of ratios and other unitless parameters, it is not limited to galactic nuclei and may be applied in a wide range of systems. Consider, for example, a planetary system. Interestingly, the forces between the S-stars and the SMBH are similar to those in a planetary system with a Sun-like star in the presence of a companion. In particular, the mass ratio between Sgr A* and the stars in the S-cluster is similar to that of a star and its planetary system. Further, the distance scales at the galactic center (SMBH and S-Star, and SMBH-companion) are roughly the square of those for a star–planet, and a star–companion. Thus, our stability timescale is also relevant in the case of planetary systems.

Significantly, observations suggest that most of the massive stars reside in binaries or higher multiples (e.g., Raghavan et al. 2006; Sana et al. 2012; Moe & Di Stefano 2017; Moe & Kratter 2021). In the planetary field, one also often considers

¹⁴ Note that other processes such as collisions and tidal capture also take place on longer timescales than the S-cluster lifetime (e.g., Rose et al. 2020, 2022); thus, the conclusion here can be extended to other physical processes beyond two-body interactions.

orbital crossing as a sign of instability (e.g., Chatterjee et al. 2008; Nagasawa & Ida 2011; Denham et al. 2019; Faridani et al. 2022; Wei et al. 2021). However, we suggest that the stability question needs to be cast as the timescale to instability in exoplanetary systems as well.

As an example, consider the bottom panel of Figure 6. This figure depicts a system with mass ratio of q=0.01 between the primary and the companion, and varies the test-particle eccentricity. Consider a system of a star and a brown dwarf companion on a circular orbit. It is thus easy to see that a circular planet (the test particle), or even a planet with a nonnegligible eccentricity on a crossing orbit, will not have its energy changed by a factor of itself for a timescale between 2000 and 10^9 orbital periods of the planet, depending on the value of α . This implies that some planetary systems may even be observed near instability. Of course, a smaller companion results in an even longer stability timescale.

A potentially relevant example may reside in the observed Kepler-419 system. This system has two massive Jupiters orbiting a $1.4\,M_\odot$ star, with $m_t=2.5\,M_J$, $e_t=0.83$, $a_t=0.37$ au, and $m_c=7.3\,M_J$, $e_c=0.18$, $a_c=1.7$ au, respectively. (e.g., Dawson et al. 2012, 2014). The system's stability has been questioned recently by Denham et al. (2019), Jackson et al. (2019). For this system, $P_t=0.19\,\mathrm{yr}$, $P_c=1.84\,\mathrm{yr}$, $T_\mathrm{peri}=0.11(P_c/2\pi)$, and our hierarchical parameter is $\alpha=0.037$. Thus, we may ask on what timescale the system's energy will change by an order of itself. Using the first line of Equation (18), we obtain $T_\mathrm{stab}\sim7\times10^4\,\mathrm{yr}$. This is shown as the red star on the bottom panel of Figure 6. Therefore, at face value, this suggests that a major change in the inner planet's energy could occur within fewer than $10^5\,\mathrm{yr}$.

We note that the inner planet cannot really be considered as a test particle in this system. However, our numerical investigation was done for a nonnegligible mass inner star and is roughly consistent with the analytical criterion (for comparable masses, our criterion underestimates the stability timescale). Thus, our stability timescale for Kepler-419 may not be far from reality.

5. Conclusion

The long-term stability of three-body systems is a fundamental problem in astrophysics with many applications, from clusters of stars in galactic nuclei to planetary systems. Furthermore, the instability of the triple systems is associated with energy exchange between the two orbits, and is a time-sensitive concept. In this paper, we develop an analytic timescale at which instability sets in for nonhierarchical triple systems. We find that numerical *N*-body experiments corroborate this analytic result. The following is a summary:

- 1. The timescale for which the system is stable, $T_{\rm stab}$, is given by Equation (18), assuming a circular companion and highly eccentric test-particle orbit in a nonhierarchical configuration. This analytic result is validated numerically in Figures 3 and 5.
- 2. For systems with such nonhierarchical configurations, the instability is primarily driven by the high susceptibility to energy change that the test particle experiences near its periapsis, rather than by close encounters between the companion and the test particle. The evolution of the test particle's orbital energy behaves like a random walk, as in Figure 2.

3. In the hierarchical limit, the random walk assumption on the energy evolution does not hold, and so the hierarchical systems are stable for much longer than predicted by Equation (18). In particular, their stability is predicted by secular evolution. The systems do not need to be strictly hierarchical for the random walk assumption to fail; they only need to be sufficiently well described by the secular approximation, such as in Figure 4. The large oscillations in the angular momentum caused by the eccentric Kozai–Lidov effect are an indicator of secular-like behavior.

Acknowledgments

E.Z. thanks Evgeni Grishin for helpful comments and discussion. S.N. acknowledges partial support from NASA ATP 80NSSC20K0505 and thanks Howard and Astrid Preston for their generous support. C.M.W. is grateful for the hospitality of the Institut d'Astrophysique de Paris, where parts of this work were carried out, and acknowledges partial support from the National Science Foundation, grant Nos. PHY 19-09247 and 22-07681.

Appendix A The Stability Timescale at Lower Eccentricities

Our analytic calculation relies on the assumption that significant changes to the test particle's energy occur near its periapsis. For this assumption to hold, it is necessary to assume a highly eccentric test-particle orbit, because of the dependence of dE/dt on the test particle's velocity, which is sharply peaked about the periapsis only for eccentric orbits. When these assumptions are violated, the analytic timescale does not strictly hold. Nevertheless, we show numerically that the analytic timescale still has some applicability at lower eccentricities.

To study the behavior of systems with low test-particle eccentricity, we integrate two sets of 1554 systems, with fixed test-particle orbital configuration and systematically varied companion orbital parameters. In one set of systems, the test particle has an initial eccentricity of 0.2, and the initial companion semimajor axis varies from 400 to 4000 au. In the other set, the test particle has an initial eccentricity of 0.5, and the initial companion semimajor axis varies from 200 to 4000 au. In both sets, the initial test-particle semimajor axis is 1020 au, the companion mass is varied from 500 to $10^6 \, M_\odot$, and the initial orbital angles of both the test particle and companion are randomly drawn uniformly in Ω , ω , f from $[0, 2\pi]$ and uniformly in $\cos i$ from [-1, 1]. All systems are integrated for $10^6 \, \text{yr}$.

Our numerical results, displayed in Figure 7, show that, for lower eccentricities, the analytic timescale overestimates the numerically calculated timescale in regions of the parameter space where orbital crossing is possible. Thus, the energy jumps at periapsis, as described in the main body of the paper, cannot fully explain the instability in the low-eccentricity regime. For a test-particle eccentricity $e_t = 0.5$, this discrepancy is not major. For e_t as low as 0.2, the disagreement becomes more severe, with the analytic result overestimating the numeric timescale by roughly a full order of magnitude.

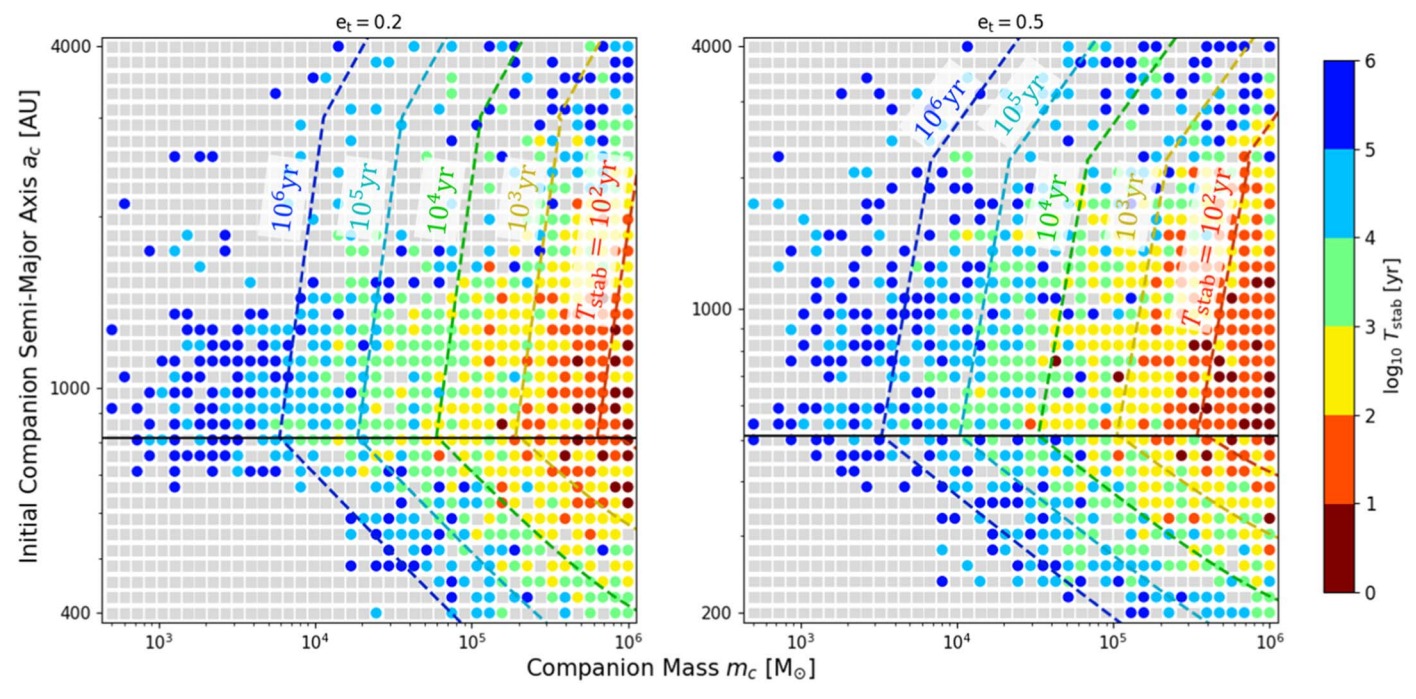


Figure 7. Stability timescale for low eccentricities. T_{stab} as a function of m_c and a_c as determined by direct N-body integration, for a test-particle star of semimajor axis 1020 au, and with eccentricities 0.2 and 0.5. The analytic timescale overestimates the numerical timescale.

Appendix B Supplemental Equations and Plots

We present supplemental equations and plots to our analytic derivation in Section 2. This section will assume familiarity with the logical framework of Section 2, but will provide additional rigor and justification for several arguments made in the section. In particular, we will derive Equation (4), the energy jump per periapsis passage, and Equations (8) and (10), the perturbing force vectors, directly from the Newtonian equations of motion, and provide additional detail for our estimate of $|f_{\rm pert}|$ for internal companions in Equation (11). We also provide an additional, more detailed, description of the time evolution of the systems studied in the paper.

B.1. The Perturbing Force

The time derivative of E, as defined by Equation (2), is, by direct differentiation,

$$\frac{dE}{dt} = \mathbf{v} \cdot \left[\frac{d^2 \mathbf{r}}{dt^2} - \frac{GM \mathbf{r}}{r^3} \right],\tag{B1}$$

where r and v are the position and velocity vectors of the test particle relative to the central body, and r is the magnitude of r.

The first term in brackets is the relative acceleration of the test particle, and the second term is equivalent to the acceleration of the test particle due to the central body. Thus, the entire quantity in brackets, which is the difference of the two, is the component of the test-particle acceleration that is not due to the central body. We call this term the perturbing force (per test mass), i.e.,

$$f_{\text{pert}} = \frac{d^2 \mathbf{r}}{dt^2} - \frac{GM\mathbf{r}}{r^3}.$$
 (B2)

When the perturbing force is defined this way, Equation (B1) is equivalent to Equation (4).

Equations (8) and (10) then follow immediately from the Newtonian equations of motion for r. For an external companion, $r = r_{tp}$, and the corresponding equation of motion is

$$\frac{d^2 \mathbf{r}_{tp}}{dt^2} = -\frac{Gm_c \mathbf{r}_{tc}}{r_{tc}^3} - \frac{Gm_p \mathbf{r}_{tp}}{r_{tp}^3} - \frac{Gm_c \mathbf{r}_{cp}}{r_{cp}^3}.$$
 (B3)

For an internal companion, $r = r_t$, and

$$\frac{d^2\mathbf{r}_t}{dt^2} = -\frac{Gm_p\mathbf{r}_{tp}}{r_{tp}^3} - \frac{Gm_c\mathbf{r}_{tc}}{r_{tc}^3}.$$
 (B4)

B.2. Estimating $|f_{pert}|$ for Internal Companions

When the companion is internal, the gravitational potential experienced by the test particle can be expanded in a multipole series, by

$$\Phi = -\frac{Gm_p}{|\mathbf{r} - \mathbf{r}_p|} - \frac{Gm_c}{|\mathbf{r} - \mathbf{r}_c|} = -\sum_{l=0}^{\infty} \frac{Ga_c^l \eta_l}{r^{l+1}} P_l(\cos \theta), \quad (B5)$$

where P_l is the Legendre polynomials, θ is the angle between the companion and the test particle's position vectors, and

$$\eta_l = \frac{m_p (-m_c)^l + m_c m_p^l}{(m_p + m_c)^l}.$$
 (B6)

The l=0 term is the potential due to the central body, so the perturbing force is the negative spatial gradient of all remaining terms, which is

$$f_{\text{pert}} = \sum_{l=2}^{\infty} \nabla \left[\frac{Ga_c^l \eta_l}{r^{l+1}} P_l(\cos \theta) \right] = \sum_{l=2}^{\infty} \frac{Ga_c^l \eta_l}{r^{l+2}} \xi_l, \quad (B7)$$

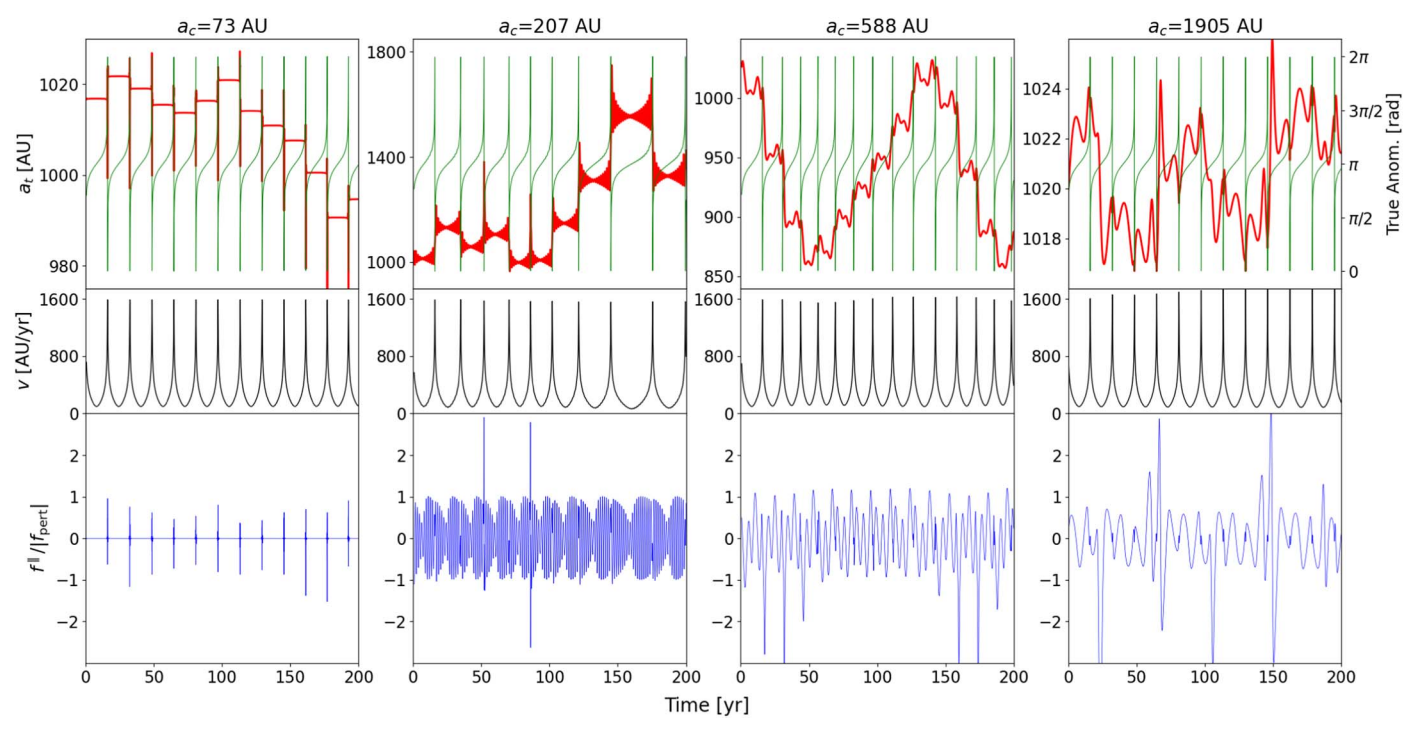


Figure 8. Additional example time evolutions of the test particle's orbit. Each column shows the evolution of a system similar to those in the DiffComp set of runs. For all systems $m_c = 27,000 \, M_{\odot}$, while a_c varies between each system. Top row: the evolution of the test particle's semimajor axis a_t (red) and true anomaly f_t (green). Middle row: the magnitude of the test particle's relative velocity, ν . Bottom row: the ratio between f^{\parallel} , the component of f_{pert} parallel to the relative test-particle velocity v, and $|f_{pert}|$, given by Equations (9) and (11).

where ξ_l is a vector, with magnitude of order unity, specifying the direction of the force, given by

$$\boldsymbol{\xi}_{l} = P'_{l}(\hat{\boldsymbol{i}} \cdot \hat{\boldsymbol{I}})[\hat{\boldsymbol{I}} - (\hat{\boldsymbol{i}} \cdot \hat{\boldsymbol{I}})\hat{\boldsymbol{i}}] - (l+1)P_{l}(\hat{\boldsymbol{i}} \cdot \hat{\boldsymbol{I}})\hat{\boldsymbol{i}}, \quad (B8)$$

where \hat{I} is the unit vector of the companion's position, and \hat{i} is the unit vector of the test particle's position.

The leading term of the remaining series is the l=2 or quadrupole term, since $\eta_1 = 0$. Then $|f_{pert}|$ is well estimated by the leading-order coefficient, $Ga_c^2 \eta_2 / r^4$, evaluated at $r = r_{\text{peri}}$, yielding Equation (11). This estimate is only good to an order of magnitude; the higher order terms, while decreasing, are not negligible since the ratio in which the series is expanded in, a_c/r , is less than unity but not small. Thus, the higher order terms contribute nontrivially to the total force, but not at a larger scale than the leading order.

B.3. The Time Evolution

Figure 8 shows additional examples of the time evolution of the test particle's orbit, for various regimes.

As was shown in Section 3.2, in all regimes, significant changes in the test particle's semimajor axis occur when its velocity peaks; that is, in a short interval near its periapsis. However, as discussed in Section 3.3, such jumps need not behave like a random walk. The two right columns in Figure 8 show systems in the quasi-secular regime. In the first system, the changes in the semimajor axis are dominated by periapsis jumps, but these jumps behave in an oscillatory manner. In the second system, the jumps are small as the companion is distant from the test particle's periapsis, so that the semimajor axis evolution is dominated by quasi-secular effects.

The bottom panels of each column indicate that the ratio between f^{\parallel} , the component of f_{pert} parallel to the relative test-particle velocity v, and our estimate $|f_{pert}|$ of the perturbing force, given by Equations (9) and (11), is of order unity. This indicates that $|f_{pert}|$ is indeed a good order-of-magnitude estimate of the perturbing force. Note that, for external companions, the estimate is valid at all points in the test particle's orbit, but for internal companions (represented by the leftmost panel in Figure 8), the estimate is only valid near periapsis, since it was derived with that assumption.

ORCID iDs

Eric Zhang https://orcid.org/0000-0002-7611-8377 Smadar Naoz https://orcid.org/0000-0002-9802-9279 Clifford M. Will https://orcid.org/0000-0001-8209-0393

References

Antognini, J. M., Shappee, B. J., Thompson, T. A., & Amaro-Seoane, P. 2014, MNRAS, 439, 1079

Antognini, J. M. O. 2015, MNRAS, 452, 3610

Antonini, F., Murray, N., & Mikkola, S. 2014, ApJ, 781, 45

Bhaskar, H., Li, G., Hadden, S., Payne, M. J., & Holman, M. J. 2020, AJ, 161, 48

Binney, J., & Tremaine, S. 2008, Galactic Dynamics: Second Edition (Princeton, NJ: Princeton Univ. Press)

Bode, J. N., & Wegg, C. 2014, MNRAS, 438, 573

Chatterjee, S., Ford, E. B., Matsumura, S., & Rasio, F. A. 2008, ApJ, 686, 580 Chen, X., & Liu, F. K. 2013, ApJ, 762, 95

Dawson, R. I., Johnson, J. A., Fabrycky, D. C., et al. 2014, ApJ, 791, 89

Dawson, R. I., Johnson, J. A., Morton, T. D., et al. 2012, ApJ, 761, 163

Denham, P., Naoz, S., Hoang, B.-M., Stephan, A. P., & Farr, W. M. 2019, S, 482, 4146

Do, T., Hees, A., Ghez, A., et al. 2019, Sci, 365, 664

Eggleton, P., & Kiseleva, L. 1995, ApJ, 455, 640

Faridani, T., Naoz, S., Wei, L., & Farr, W. M. 2022, ApJ, 932, 78

Fragione, G., Kocsis, B., Rasio, F. A., & Silk, J. 2022, ApJ, 927, 231

Fragione, G., Loeb, A., Kremer, K., & Rasio, F. A. 2020, ApJ, 897, 46

Generozov, A., & Madigan, A.-M. 2020, ApJ, 896, 137

```
Ghez, A. M., Salim, S., Hornstein, S. D., et al. 2005, ApJ, 620, 744
Ghez, A. M., Wright, S. A., Matthews, K., et al. 2004, ApJL, 601, L159
Gillessen, S., Eisenhauer, F., Trippe, S., et al. 2009, ApJ, 692, 1075
Gillessen, S., Genzel, R., Fritz, T. K., et al. 2012, Natur, 481, 51
Gillessen, S., Plewa, P. M., Eisenhauer, F., et al. 2017, ApJ, 837, 30
Ginat, Y. B., & Perets, H. B. 2021a, MNRAS, 508, 190
Ginat, Y. B., & Perets, H. B. 2021b, PhRvX, 11, 031020
GRAVITY Collaboration, Abuter, R., Amorim, A., et al. 2018, A&A,
   615, L15
GRAVITY Collaboration, Abuter, R., Amorim, A., et al. 2020, A&A, 636, L5
Grishin, E., Perets, H. B., & Fragione, G. 2018, MNRAS, 481, 4907
Grishin, E., Perets, H. B., Zenati, Y., & Michaely, E. 2016, MNRAS, 466, 276
Gualandris, A., & Merritt, D. 2009, ApJ, 705, 361
Gürkan, M. A., & Rasio, F. A. 2005, ApJ, 628, 236
Hamilton, D. P., & Burns, J. A. 1991, Icar, 92, 118
Hansen, B. M. S., & Milosavljević, M. 2003, ApJL, 593, L77
Hayashi, T., Trani, A. A., & Suto, Y. 2022, ApJ, 939, 81
Hayashi, T., Trani, A. A., & Suto, Y. 2023, ApJ, 943, 58
Hills, J. G. 1988, Natur, 331, 687
Ivanov, P. B., Polnarev, A. G., & Saha, P. 2005, MNRAS, 358, 1361
Jackson, J. M., Dawson, R. I., & Zalesky, J. 2019, AJ, 157, 166
Katz, B., & Dong, S. 2012, arXiv:1211.4584
Kol, B. 2021, CeMDA, 133, 17
Kozai, Y. 1962, AJ, 67, 591
Lidov, M. L. 1962, P&SS, 9, 719
Lithwick, Y., & Naoz, S. 2011, ApJ, 742, 94
Lu, J. R., Do, T., Ghez, A. M., et al. 2013, ApJ, 764, 155
Lu, J. R., Ghez, A. M., Hornstein, S. D., et al. 2009, ApJ, 690, 1463
Luo, L., Katz, B., & Dong, S. 2016, MNRAS, 458, 3060
Maillard, J. P., Paumard, T., Stolovy, S. R., & Rigaut, F. 2004, A&A,
   423, 155
Manwadkar, V., Kol, B., Trani, A. A., & Leigh, N. W. C. 2021, MNRAS,
   506, 692
Mardling, R. A., & Aarseth, S. J. 2001, MNRAS, 321, 398
Moe, M., & Di Stefano, R. 2017, ApJS, 230, 15
Moe, M., & Kratter, K. M. 2021, MNRAS, 507, 3593
```

```
Murray, C. D., & Dermott, S. F. 2000, in Solar System Dynamics, ed.
  C. D. Murray & S. F. Dermott (Cambridge: Cambridge Univ. Press)
Mushkin, J., & Katz, B. 2020, MNRAS, 498, 665
Mylläri, A., Valtonen, M., Pasechnik, A., & Mikkola, S. 2018, MNRAS,
  476, 830
Nagasawa, M., & Ida, S. 2011, ApJ, 742, 72
Naoz, S., Farr, W. M., Lithwick, Y., Rasio, F. A., & Teyssandier, J. 2013a,
  MNRAS, 431, 2155
Naoz, S., Kocsis, B., Loeb, A., & Yunes, N. 2013b, ApJ, 773, 187
Naoz, S., Li, G., Zanardi, M., de Elía, G. C., & Di Sisto, R. P. 2017, AJ,
  154, 18
Naoz, S., & Silk, J. 2014, ApJ, 795, 102
Naoz, S., Will, C. M., Ramirez-Ruiz, E., et al. 2020, ApJL, 888, L8
Petrovich, C. 2015, ApJ, 808, 120
Poisson, E., & Will, C. M. 2014, Gravity: Newtonian, Post-Newtonian,
  Relativistic (Cambridge: Cambridge Univ. Press)
Raghavan, D., Henry, T. J., Mason, B. D., et al. 2006, ApJ, 646, 523
Rashkov, V., & Madau, P. 2014, ApJ, 780, 187
Rauch, K. P., & Hamilton, D. P. 2002, AAS Meeting, 33, 08.02
Rose, S. C., Naoz, S., Gautam, A. K., et al. 2020, ApJ, 904, 113
Rose, S. C., Naoz, S., Sari, R., & Linial, I. 2022, ApJL, 929, L22
Roy, A., & Haddow, M. 2003, CeMDA, 87, 411
Sabha, N., Eckart, A., Merritt, D., et al. 2012, A&A, 545, A70
Sana, H., de Mink, S. E., de Koter, A., et al. 2012, Sci, 337, 444
Stone, N. C., & Leigh, N. W. C. 2019, Natur, 576, 406
The LIGO Scientific Collaboration, The Virgo Collaboration, Abbott, R., et al.
  2020a, PhRvL, 125, 101102
The LIGO Scientific Collaboration, The Virgo Collaboration, Abbott, R., et al.
  2020b, ApJL, 900, L13
Tory, M., Grishin, E., & Mandel, I. 2022, PASA, 39, e062
Vynatheya, P., Hamers, A. S., Mardling, R. A., & Bellinger, E. P. 2022,
         S, 516, 4146
Wei, L., Naoz, S., Faridani, T., & Farr, W. M. 2021, ApJ, 923, 118
Will, C. M. 2021, PhRvD, 103, 063003
Yelda, S., Ghez, A. M., Lu, J. R., et al. 2014, ApJ, 783, 131
Zheng, X., Lin, D. N. C., & Mao, S. 2020, ApJ, 905, 169
```